Physica B 407 (2012) 4686–4694

Contents lists available at SciVerse ScienceDirect

Physica B

journal homepage: www.elsevier.com/locate/physb

Structural and optical studies of $FeSb_2$ under high pressure

C.M. Poffo [a], S.M. Souza [a,1], D.M. Trichês [a,1], J.C. de Lima [b,*], T.A. Grandi [b], A. Polian [c], M. Gauthier [c]

[a] Departamento de Engenharia Mecânica, Universidade Federal de Santa Catarina, Campus Universitário Trindade, S/N, C.P. 476, 88040-900 Florianópolis, Santa Catarina, Brazil
[b] Departamento de Física, Universidade Federal de Santa Catarina, Campus Universitário Trindade, S/N, C.P. 476, 88040-900 Florianópolis, Santa Catarina, Brazil
[c] Physique des Milieux Denses, IMPMC, CNRS-UMR 7590, Université Pierre et Marie Curie-Paris 6, B115, 4 Place Jussieu, 75252 Paris Cedex 05, France

ARTICLE INFO

Article history:
Received 13 August 2012
Received in revised form
21 August 2012
Accepted 22 August 2012
Available online 31 August 2012

Keywords:
Nanocrystals
Thermoelectric materials
Mechanical alloying
X-ray diffraction
Raman spectroscopy
High pressure

ABSTRACT

Nanostructured orthorhombic $FeSb_2$ was formed along with an amorphous phase, by mechanical alloying from a mixture of Fe and Sb powders. The influence of pressure on the structural and optical properties of the material was investigated by X-ray diffraction (XRD) and Raman spectroscopy (RS) up to 28.2 and 45.2 GPa, respectively. The volume fraction of the amorphous phase increased with increasing pressure. For pressures above 14.3 GPa, a tetragonal $FeSb_2$ phase was also observed. For the orthorhombic $FeSb_2$ phase, the pressure dependence of the volume fitted to a Birch–Murnaghan equation of state gave a bulk modulus $B_0=75.5\pm3.2$ GPa, and its derivative $B_0'=7.2\pm0.7$. For the orthorhombic $FeSb_2$ phase, the Raman active A_g^2 mode was observed up to 28.3 GPa, while the B_{1g}^2 mode was not for pressures larger than 14 GPa. For pressures above 21 GPa, the Raman active A_{1g} mode of a tetragonal $FeSb_2$ phase was observed.

1. Introduction

$FeSb_2$ is a narrow gap semiconductor that has attracted attention because of its unusual magnetic properties (paramagnetic to diamagnetic crossover at about 100 K), thermoelectric properties (colossal Seebeck coefficient S at 10 K and the largest power factor $S^2\sigma$ ever reported) [1], and transport properties (a metal-to-semiconductor transition at about 40 K) [2].

Under ambient conditions, $FeSb_2$ crystallizes in an orthorhombic structure (S.G. Pnnm, $Z=2$), with Fe atoms at the 2a (0,0,0) Wyckoff position and Sb atoms at the 4g (x,y,0) position, with $x=0.1885$ and $y=0.3561$. Each Fe atom in a deformed octahedral environment and octahedra share edges along the c-axis [3]. Fig. 1 shows the conventional unit cell for $FeSb_2$. The angles [Sb(10)–Fe(7)–Sb(11)] and [Sb(10)–Fe(7)–Sb(12)] are supplementary, with values of 91.64° and 88.36°, respectively. The interatomic distances Sb(10)–Sb(11) and Sb(10)–Sb(12) are 3.712 Å and 3.607 Å, respectively, while the Fe(7)–Sb(2), Fe(7)–Sb(3), Fe(7)–Sb(11) and Fe(7)–Sb(12) distances are 2.601 Å and Fe(7)–Sb(6) and Fe(7)–Sb(10) distances are 2.575 Å.

The influence of pressure on bulk $FeSb_2$ was studied by Petrovic et al. [4] for pressures up to 7.14 GPa and no structural changes were observed. On the other hand, Wu et al. [5], using ab initio calculations, predicted a transformation of the orthorhombic phase into a tetragonal structure ($CuAl_2$ structure type) at 38 GPa.

It has been suggested in the literature that the thermoelectric conversion efficiency of a material can be improved by reducing the crystallite size to nanometric dimensions (<100 nm). For some years, our research has been focused on nanostructured materials because of their unique properties and, more recently, we studied the influence of high pressure on nanostructured materials, especially those with thermoelectric applications [6–10].

From the structural point of view, nanostructured materials have two components: one crystalline, made of crystallites with nanometric dimensions (<1000 Å), with the same structure as the bulk counterparts, and another interfacial, made of different types of defects (grain boundaries, interphase boundaries, dislocations, etc.). The number of atoms in both components is similar, causing a strong dependence of the properties on the atomic arrangements present in the interfacial component [11]. Nanostructured materials have been produced by different techniques, including mechanical alloying (MA). Suryanarayana's paper [12] gives a good review of the MA technique, while the physical mechanisms involved are described in Refs. [13–16].

A stoichiometric $FeSb_2$ mixture was subjected to the MA technique for 32 h, which resulted in a nanostructured orthorhombic $FeSb_2$ phase, an amorphous phase, and a small amount of unreacted Sb. The effect of high pressure on the resulting material was investigated by X-ray diffraction (XRD) and Raman spectroscopy (RS); the results obtained are reported in the following sections.

* Corresponding author. Tel.: +55 48 37212847; fax: +55 48 37219946.
E-mail address: fsc1jcd@fisica.ufsc.br (J.C. de Lima).
[1] Present address: Departamento de Física, Universidade Federal do Amazonas, 3000 Japiim, 69077-000 Manaus, Amazonas, Brazil.

0921-4526/$ - see front matter © 2012 Elsevier B.V. All rights reserved.
http://dx.doi.org/10.1016/j.physb.2012.08.032

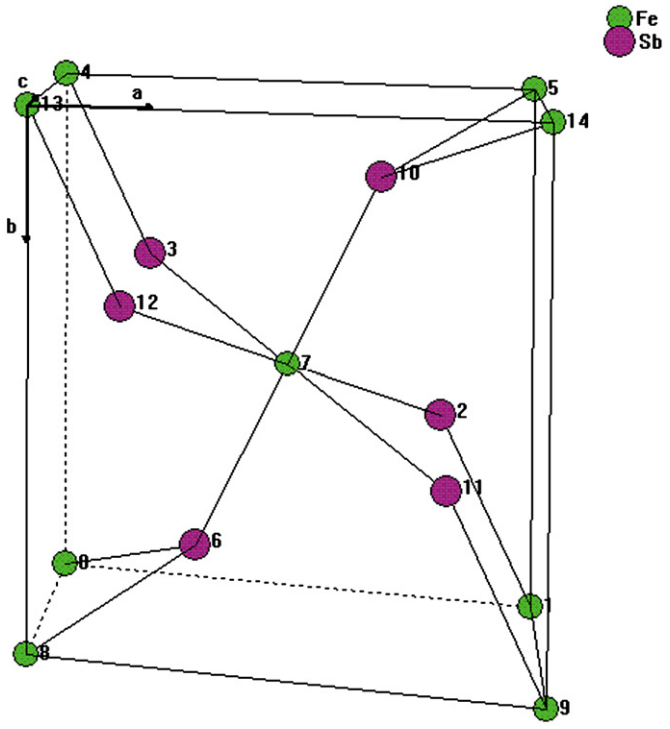

Fig. 1. Conventional unit cell of $FeSb_2$. The angles Sb(10)–Fe(7), Sb(12) and Sb(10)–Fe(7)–Sb(11) are supplementary.

2. Experimental procedure

A 1:2 mixture of Fe (Aldrich, purity 99.999%) and Sb (Alfa Aesar, purity 99.999%) was sealed together with several steel balls of 11.0 mm in diameter in a cylindrical steel vial under argon atmosphere. The ball-to-powder weight ratio was 7:1. The vial was mounted on an SPEX mixer/mill, model 8000. The temperature was kept close to room temperature by a ventilation system. After 32 h of milling, the XRD pattern showed an excellent agreement with that given in the ICSD Database (code 41727) [3] for the orthorhombic $FeSb_2$ phase. An amorphous phase was also observed, along with a small amount of unreacted Sb.

A diamond anvil cell (DAC) with an opening that allowed probing up to $2\theta=28^\circ$ was used [17]. A small amount of $FeSb_2$ powder was compacted between diamonds to a final thickness of approximately 15 μm. A small chip of this preparation, about 80 μm in diameter, was loaded into a stainless-steel gasket hole of 150 μm diameter. Neon gas was used as a pressure-transmitting medium. The pressure was determined by the fluorescence shift of a ruby sphere loaded in the sample chamber [18]. The quasi-hydrostatic conditions were controlled throughout the experiments by monitoring the separation and width of R_1 and R_2 lines. In situ XRD patterns as a function of pressure were acquired at the XRD1 station of the ELETTRA synchrotron radiation facility. This diffraction beamline is designed to provide a monochromatized, high-flux, tunable X-ray source in the spectral range from 4 to 25 keV [19]. The study was performed using a wavelength of 0.68881 Å ($E=18{,}002.06$ eV). The detector was a 345-mm imaging plate from MarResearch. The sample-to-detector distance was calibrated using diffraction data from Si powder loaded in the diamond anvil cell. The XRD data were collected at 0.7, 2.2, 3.7, 5.3, 6.6, 8.1, 9.7, 12.6, 14.3, 15.6, 17.6, 19.1, 21.0, 23.3 and 28.2 GPa. An exposure time of 10 min was used for all measurements. The two-dimensional diffraction patterns were converted to intensity versus 2θ using the fit2D software [20] and analyzed by the Rietveld method [21] using the GSAS package [22].

For the Raman measurements, a particle of approximately $50\times60\times20\ \mu m^3$ was loaded in the DAC. The Raman spectra and ruby luminescence were recorded in the backscattering geometry by means of a Jobin-Yvon T64000 Raman triple spectrometer and a multichannel CCD detector. An excitation line of $\lambda=514.5$ nm of an Ar laser was used for excitation and focused down to 5 μm with a power of about 20 mW at the entrance of the DAC. With increasing pressure, Raman spectra were collected at 1.3, 5.3, 7.5, 9.6, 12.7, 14.0, 21.0, 24.9, 28.3, 32.4, 36.9, 42.7 and 45.2 GPa. With decreasing pressure, Raman spectra were collected at 0.4, 9.3, 15.3, 22.9, 36.7 and 40.8 GPa. An exposure time of 120 min was used for all measurements. The Raman frequencies were determined from a fit of the peaks to a Lorentzian profile. The frequency accuracy was better than 1 cm^{-1}.

3. Results and discussion

3.1. Characterization of the as-milled powder

The XRD pattern for 32 h of milling showed an excellent agreement with that given in the ICSD Database (code 41727) [3] for orthorhombic $FeSb_2$ (S.G. Pnnm, $Z=2$). The diffraction peaks of elemental Sb were also seen, indicating that a small content of elemental Sb remained unreacted. From the Rietveld analysis, a volume fraction of 7% Sb was obtained.

The structural stability of the as-milled powder was investigated by performing two sequential differential scanning calorimetry measurements. The first measurement showed an intense exothermic peak located at about 338 °C, which was associated with crystallization of an amorphous phase, while in the second measurement this peak was absent. This result showed that, besides the $FeSb_2$ phase, an amorphous phase was also formed.

The mean size of the crystallites of the $FeSb_2$ phase was estimated using the Scherrer formula [23]. For this, the full-width at half-maximum (FWHM) β in radians and 2θ values of the most intense peaks obtained from the Rietveld refinement of measured XRD pattern were used, and a value of 245 Å was obtained.

The volume fractions of crystalline ($FeSb_2$ and Sb) and interfacial/amorphous components forming the microstructure were estimated. For this, the measured XRD pattern was normalized to electrons unit using a procedure described in Refs. [24,25], and values of $\approx 63\%$ and 37% were estimated, respectively.

Heat treatments on the as-milled samples were performed at 250 °C and 400 °C. Rietveld analysis of XRD patterns for annealed samples showed formation of Fe_3O_4 as well as decomposition of $FeSb_2$. The structural, optical, thermal, and photoacoustic properties of the as-milled and annealed powder at room conditions were studied and the results will be published elsewhere.

3.2. High pressure XRD measurements

Figs. 2 and 3 show in situ synchrotron XRD patterns of the nanostructured as-milled powder up to the highest pressure used (28.2 GPa). No XRD measurements were performed for decreasing pressure. The XRD pattern measured at 0.7 GPa showed an excellent agreement with that given in the ICSD Database (code 41727) [3] for the orthorhombic $FeSb_2$ phase (S.G. Pnnm, $Z=2$). Diffraction peaks corresponding to the elemental Sb (marked with symbol "*" in Fig. 2) were also observed. With increasing pressure, all the diffraction peaks shifted toward higher 2θ values and the peaks between $2\theta=13.5^\circ$ and 16° became well separated. The peaks of elemental Sb were observed only up to 9.7 GPa. Neon gas was used as pressure-transmitting medium, and, according to the literature, it crystallizes in a f.c.c structure at about 10 GPa [26]. Thus, the peak seen at about $2\theta=19.7^\circ$ on the XRD pattern at

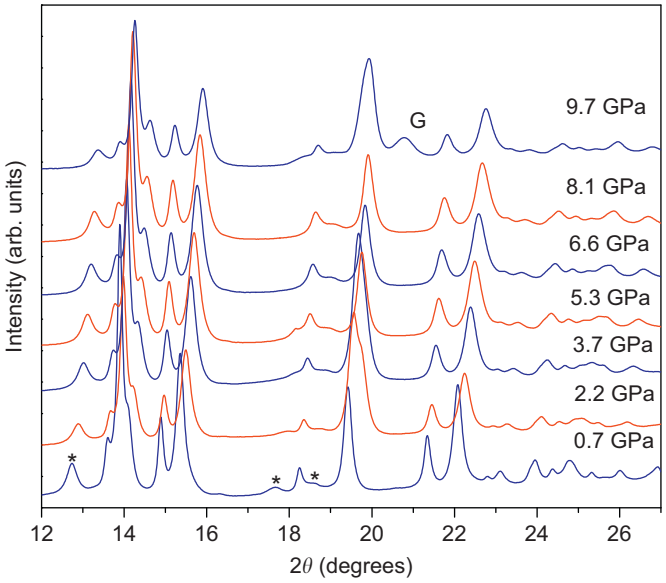

Fig. 2. XRD patterns measured with increasing pressure up to 9.7 GPa for nanostructured orthorhombic $FeSb_2$ powder. The diffraction peaks of elemental Sb are marked with the asterisk (*) symbol, while that from the gasket is identified by the *G* letter.

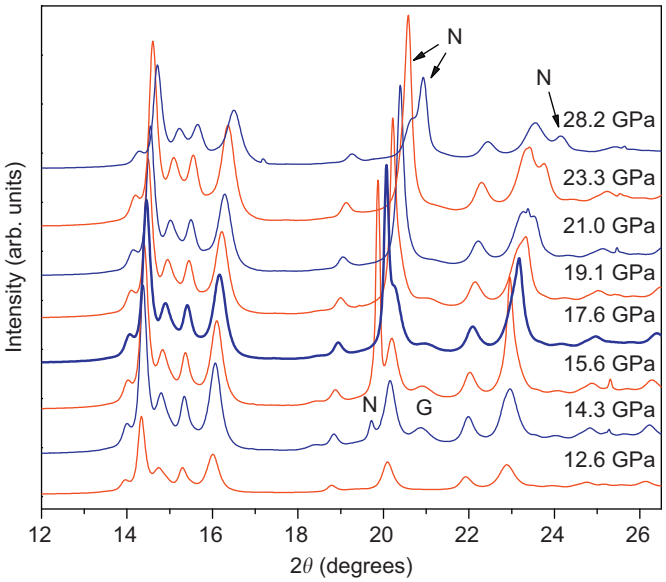

Fig. 3. XRD patterns measured with increasing pressure from 12.6 to 28.2 GPa for the nanostructured orthorhombic $FeSb_2$ powder. The diffraction peaks from the gasket and from neon are identified by the G and N letters, respectively.

14.3 GPa was indexed to the (1 1 1) plane of cubic neon. This peak is marked with the letter N in Fig. 3. With increasing pressure, other peaks corresponding to solid neon are observed. The peak seen at about $2\theta = 20.8^\circ$ (marked with the letter G) on the XRD pattern at 9.7 GPa is attributed to the gasket, since is was observed after removing the sample. It is also seen on the patterns at 14.3, 15.6, 17.6 and 19.1 GPa.

In Figs. 2 and 3, between $2\theta = 13.5^\circ$ and 17°, there is a halo of an amorphous phase. Visually, one can see that its volume fraction increases with increasing pressure, reaching the maximum intensity at about 23.3 GPa. In another study performed on this same powder, whose results are mentioned in Section 3.1, an amorphous phase was also observed and investigated. In the present study, the evolution of amorphous phase with increasing pressure was investigated. For this, the software DATLAB code [27] was used to estimate its volume fraction at 6.6, 14.3, 23.3 and 28.2 GPa, and the result is shown in Fig. 4. This figure shows that the intensity of the halo is maximum at 23.3 GPa, indicating that the volume fraction of the amorphous phase increases with increasing pressure up to this pressure. When the pressure is increased to 28.2 GPa, the intensity of the halo decreases, suggesting that a new high pressure phase is formed. The diffuse scattering increases for angles larger than $2\theta = 18^\circ$. This increase is attributed to the Fe K_α and/or K_β fluorescence generated during the measurements, since the photon energy was 18,002.06 eV and the Fe *K*-edge was 7112 eV. The effect of pressure on the local atomic structure, i.e., on the average interatomic distance of the first neighbors, was evaluated using the Ehrenfest relation $r = \lambda/E\sin\theta$ [28], where the structure dependent constant E was taken to be 1.671, θ is the half-angle of main diffraction halo and λ is the wavelength used in the experiments. For the pressures of 6.6, 14.3, 23.3 and 28.2 GPa, average interatomic distances of 3.20, 3.12, 3.05 and 2.95 Å were obtained, respectively. These values decrease with increasing pressure, as expected, and are compatible with the interatomic distances for Fe–Sb alloys, since the atomic radii of Fe and Sb are 1.24 and 1.82 Å, respectively [29].

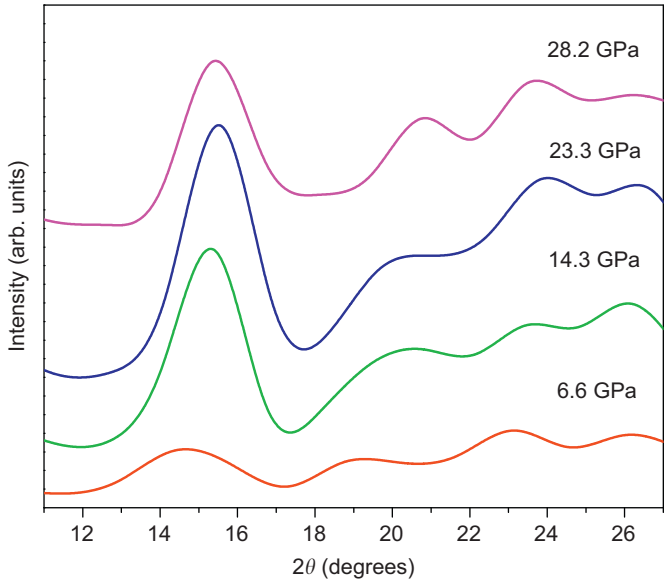

Fig. 4. Estimated XRD scattering for the amorphous phase for several pressures.

In order to understand the increase in the volume fraction of amorphous phase with increasing pressure, the pressure dependence of the mean size of the crystallites was estimated using the Scherrer formula [23]. For this, the XRD patterns were refined and simulated through the Rietveld method [21,22]. From the refinement, the full-width at half-maximum (FWHM) β in radians and 2θ values of the most intense peak for $FeSb_2$ were used. Fig. 5 shows the mean size of the crystallites for several pressures. The solid line is only a guide to the eye. From this figure, one can see that the $FeSb_2$ phase produced by the MA technique is nanostructured. With increasing the pressure up to 0.7 GPa, the volume fraction of $FeSb_2$ increases, and this can be explained by the following argument: the increase in pressure first promotes a reduction of the interfacial component through partial elimination of the several types of defects. In addition, atoms located near the boundaries of the crystallites are incorporated, promoting their growth. Also, strains present in the crystalline component are eliminated. All these processes improve the crystallinity of the nanostructured $FeSb_2$ phase, leaving it energetically more stable. Increasing pressure further, an initial fast decrease up to 5.3 GPa, a smooth decrease up to 12.6 GPa, a maximum at around 14.3 GPa, and a fast decrease thereafter can be observed. These results show

that, with increasing pressure, decomposition of the $FeSb_2$ phase occurs. Thus, the increase of the volume fraction of the amorphous phase with increasing pressure seen in Fig. 4 can be associated with decomposition of the $FeSb_2$ phase and/or elimination of the interfacial component.

The XRD patterns displayed in Figs. 2 and 3 for the orthorhombic $FeSb_2$ phase were refined, and the structural parameters are summarized in Table 1. To illustrate the quality of the refinements, the experimental and simulated XRD patterns at 0.7 GPa are shown in Fig. 6.

The pressure dependence of the lattice parameters is shown in Fig. 7, where one can see two regions denoted as I and II: Up to 9.7 GPa (region I), the lattice parameters a–c follow a second degree polynomial, while for higher pressures (region II) they follow a linear polynomial as showed by the fits (solid lines). Individual lattice parameter compressibilities $\beta_0^i = -(1/i)(\partial i/\partial P)_T$ $(i=a,b,c)$ were calculated, and the results were $\beta_0^a = 0.00330(9)\ \mathrm{GPa}^{-1}$, $\beta_0^b = 0.00490(5)\ \mathrm{GPa}^{-1}$ and $\beta_0^c = 0.00706(6)\ \mathrm{GPa}^{-1}$ for region I and $\beta_0^a = 0.00153(4)\ \mathrm{GPa}^{-1}$, $\beta_0^b = 0.00159(2)\ \mathrm{GPa}^{-1}$ and $\beta_0^c = 0.00199(9)\ \mathrm{GPa}^{-1}$ for region II. In both regions, the c-axis is more compressive than the a- and b-axis. The calculated values for region I agree well with those reported in Ref. [4] for a maximum pressure of 7.14 GPa.

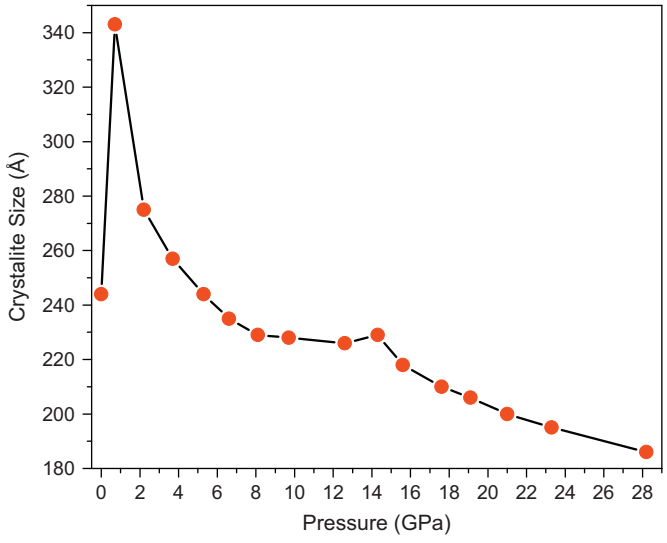

Fig. 5. Mean crystallite size of orthorhombic $FeSb_2$ phase for increasing applied pressures.

The volume as a function of pressure $V(P)$ obtained from the Rietveld refinement for the orthorhombic $FeSb_2$ phase (see Table 1) was fitted to a Birch–Murnaghan equation of state (BM EOS) [30]:

$$P = \frac{3}{2}B_0X^5(X^2-1)\left\{1+\frac{3}{4}(B_0'-4)(X^2-1)\right\} \quad (1)$$

where $X=(V_0/V)^{1/3}$. The value $V_0 = 122.27\ \text{Å}^3$ was obtained from the Rietveld refinement of XRD pattern measured at ambient

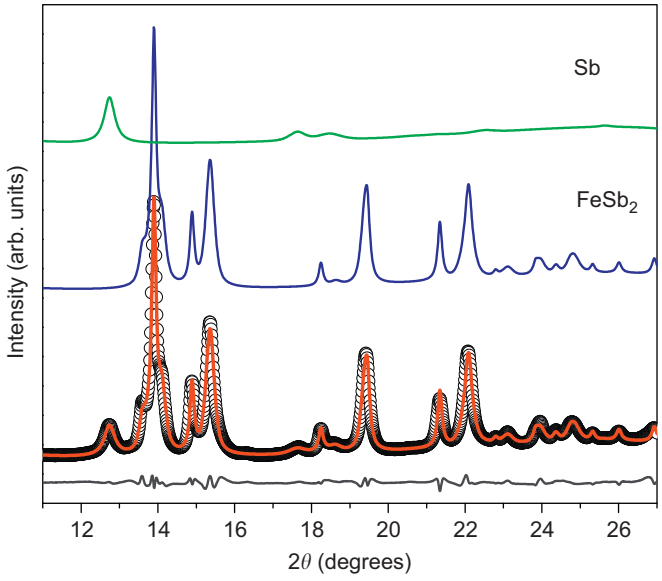

Fig. 6. XRD pattern of the orthorhombic $FeSb_2$ phase at 0.7 GPa (open circles). Other colored solid lines represent the Rietveld simulations. The bottom line is the residual intensity. (For interpretation of the references to color in this figure legend, the reader is referred to the web version of this article.)

Table 1
Orthorhombic $FeSb_2$ high pressure refinements: lattice parameters, volume, Fe atom at 2a site at (0,0,0), coordinates x and y of the Sb atom at 4g site at (x,y,0), interatomic distances Fe–Sb and angle Fe–Sb–Fe.

P **(GPa)**	**0.7**	**2.2**	**3.7**	**5.3**	**6.6**	**8.1**	**9.7**	**12.6**
a **(Å)**	5.8193	5.7898	5.7610	5.7440	5.7213	5.7100	5.6829	5.6698
b **(Å)**	6.5323	6.4878	6.4498	6.4233	6.3938	6.3722	6.3593	6.3175
c **(Å)**	3.2008	3.1698	3.1418	3.1237	3.0996	3.0875	3.0747	3.0553
V **(Å^3)**	121.67(3)	119.06(7)	116.74(0)	115.25(0)	113.38(6)	112.33(9)	111.11(7)	109.43(7)
Sb (*x*)	0.1878(3)	0.1909(7)	0.1894(8)	0.1865(9)	0.1897(3)	0.1909(1)	0.1906(1)	0.1915(9)
Sb (*y*)	0.3565(8)	0.3591(7)	0.3564(2)	0.3548(3)	0.3524(3)	0.3531(7)	0.3533(5)	0.3447(8)
Fe–Sb *x* 2 (Å)	2.5729(2)	2.5582(6)	2.5447(8)	2.5184(5)	2.5009(5)	2.5007(3)	2.4947(8)	2.4341(3)
Fe–Sb *x* 4 (Å)	2.5957(2)	2.5791(6)	2.5544(7)	2.5592(7)	2.5385(5)	2.5245(4)	2.5147(9)	2.5204(2)
Fe–Sb–Fe (°)	128.60(2)	128.48(3)	128.89(7)	128.98(6)	129.67(3)	129.65(9)	129.60(6)	131.12(7)
P **(GPa)**	**14.3**	**15.6**	**17.6**	**19.1**	**21**	**23.3**	**28.2**	
a **(Å)**	5.6564	5.6501	5.6234	5.6079	5.5931	5.5776	5.5325	
b **(Å)**	6.2990	6.2841	6.2708	6.2479	6.2248	6.2027	6.1577	
c **(Å)**	3.0392	3.0334	3.0191	3.0100	2.9982	2.9810	2.9548	
V **(Å^3)**	108.28(5)	107.70(3)	106.46(3)	105.46(3)	104.38(5)	103.13(1)	100.66(2)	
Sb (*x*)	0.1946(1)	0.1947(1)	0.1827(2)	0.1952(9)	0.1990(3)	0.1937(8)	0.1899(8)	
Sb (*y*)	0.3504(3)	0.3509(5)	0.3548(5)	0.3497(5)	0.3525(8)	0.3517(7)	0.3504(1)	
Fe–Sb *x* 2 (Å)	2.4664(2)	2.4648(2)	2.4506(4)	2.4445(8)	2.4338(1)	2.4351(7)	2.4001(0)	
Fe–Sb *x* 4 (Å)	2.4862(2)	2.4804(5)	2.5082(9)	2.4628(1)	2.4609(5)	2.4461(0)	2.4439(3)	
Fe–Sb–Fe (°)	130.48(6)	130.40(4)	128.88(7)	130.65(4)	130.47(2)	130.29(0)	130.25(6)	

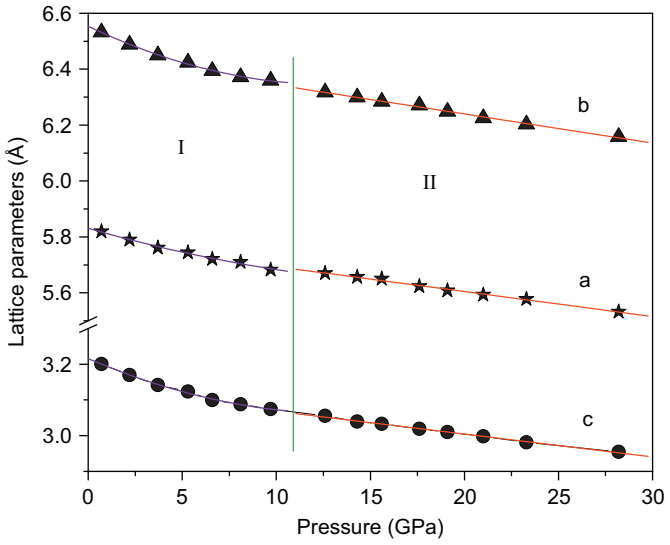

Fig. 7. Pressure dependence of the lattice parameters of the orthorhombic $FeSb_2$ phase.

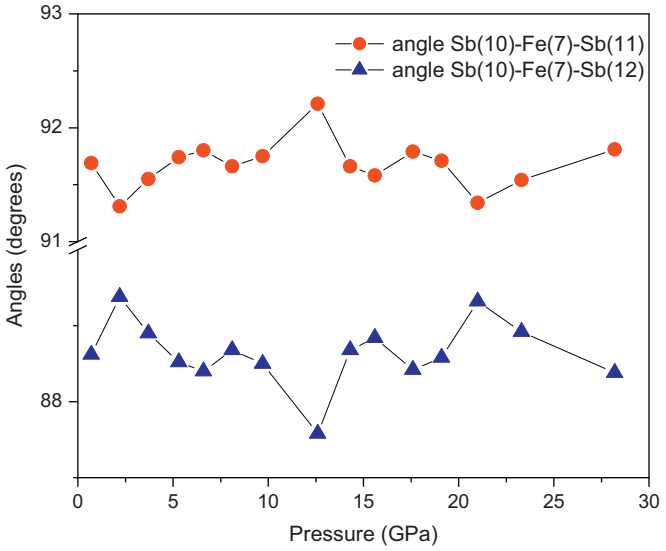

Fig. 9. Pressure dependence of the angles Sb(10)–Fe(7) Sb(12) and Sb(10)–Fe(7)–Sb(11).

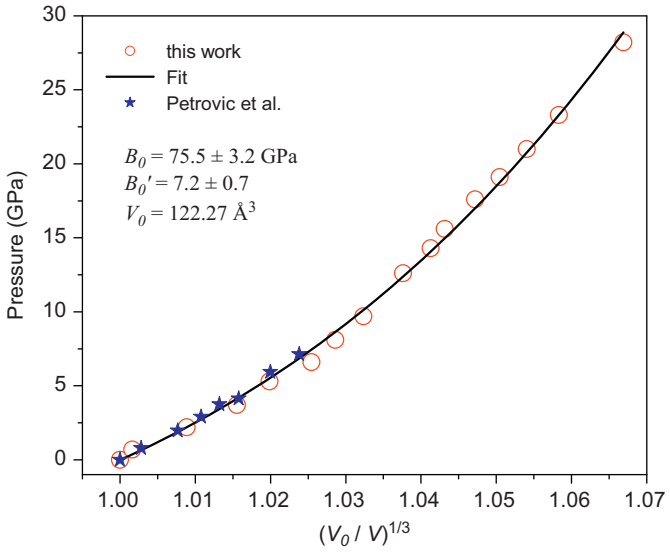

Fig. 8. Pressure dependence of the volume of the nanostructured orthorhombic $FeSb_2$ phase deduced from Rietveld refinements. Present study (open circles) and results from Ref. [4] (full stars). The solid line is the fit to a Birch–Murnaghan equation of state.

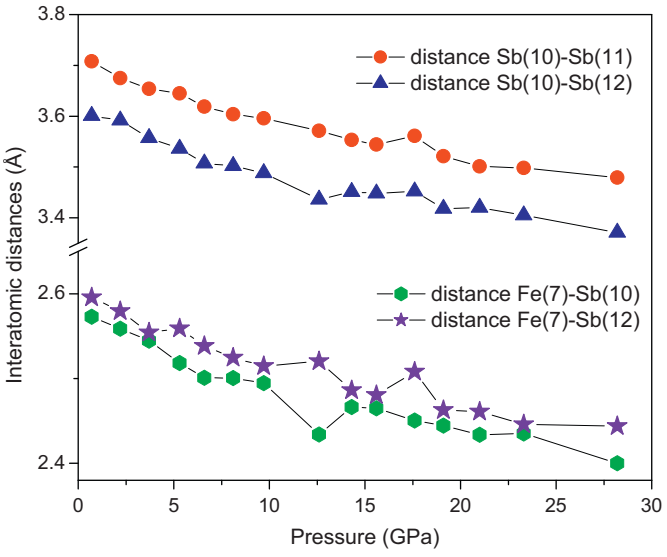

Fig. 10. Pressure dependence of the interatomic distances Sb(10)–Sb(11), Sb(10)–Sb(12), Fe(7)–Sb(10) and Fe(7)–Sb(12).

conditions. The fitting procedure yielded $B_0 = 75.5 \pm 3.2$ GPa and $B_0' = 7.2 \pm 0.7$, as shown in Fig. 8. For bulk $FeSb_2$, Petrovic et al. [4] reported the values $B_0 = 84(3)$ GPa and $B_0' = 5(1)$, and their data are also shown in Fig. 8 (open stars), while Wu et al. [5] reported the values $B_0 = 94$ GPa, $B_0' = 4.9$ and $B_0 = 68$ GPa, $B_0' = 5.9$ for $FeSb_2$ crystallized in Pnnm and I4/mcm structures, respectively. According to Fecht [31], the bulk modulus B_0 for nanometric metals decreases with increasing volume fraction of the interfacial component. Thus, the difference between B_0 values obtained in this study and those reported in Refs. [4,5] can be due to the fact that our sample is nanostructured.

The influence of pressure on the angles [Sb(10)–Fe(7)–Sb(11)] and [Sb(10)–Fe(7)–Sb(12)] as well as on the interatomic distances Sb(10)–Sb(11), Sb(10)–Sb(12), Fe(7)–Sb(10) and Fe(7)–Sb(12) was also investigated and is shown in Figs. 9 and 10, respectively. The interatomic distances are associated with the Raman active modes of $FeSb_2$ that will be discussed later. For this, the refined structural parameters listed in Table 1 were used together with the Crystal Office 98 Software [32] to build a 3D structure. From Fig. 9, one can see the angles [Sb(10)–Fe(7)–Sb(12)] and [Sb(10)–Fe(7)–Sb(11)] show a minimum and a maximum, respectively, at 12.6 GPa. The interatomic distances Sb(10)–Sb(12) and Fe(7)–Sb(10) display a minimum at 12.6 GPa, while Fe(7)–Sb(12) shows a maximum at this pressure. The minimum and maximum occur in a pressure close to 14.3 GPa, where the mean size of the crystallites displays a maximum (see Fig. 5). These results suggest a significant structural change at about 14.3 GPa.

Under ambient conditions, $TiSb_2$, VSb_2, $MnSn_2$, $CoSn_2$ and $FeSn_2$ crystallize in the $CuAl_2$ structure type [3]. Using first-principle calculations based on the density functional theory within the generalized gradient approximation, Wu et al. [5] predicted a $FeSb_2$ orthorhombic–tetragonal ($CuAl_2$ structure-type) phase transition at 38 GPa. In another study, Takizawa et al. [33] reported the formation of a high pressure $CrSb_2$ phase, crystallized in a $CuAl_2$ structure-type, at a temperature of 500 °C and pressures above 5.5 GPa. Based on

these results, we examined the formation of a new $FeSb_2$ phase with the $CuAl_2$ structure-type at about 14.3 GPa. For this, the structural data for the high pressure $CrSb_2$ phase, together with the classical relationship among interplanar distances, Muller indexes, lattice parameters and the Bragg law [23] were used. The diffraction peaks located at about $2\theta = 14.96^\circ$ and 18.31°, represented by shoulders on the XRD pattern measured at 14.3 GPa, were indexed to the (2 1 1) and (3 1 0) planes, respectively, for calculated lattice parameters $a = 6.8441$ Å and $c = 5.2563$ Å. In order to compare a possible formation of a new high pressure $FeSb_2$ phase with the $CuAl_2$ structure-type, Fig. 11 shows the XRD pattern measured at 14.3 GPa with the XRD pattern given in ICSD Database (code 42521) [3] for the tetragonal VSb_2 phase, using the lattice parameters obtained above. The XRD pattern of VSb_2 was multiplied by an arbitrary factor to facilitate the comparison.

It is interesting to note that for pressures between 14.3 and 24.3 GPa, the volume fraction of the tetragonal $FeSb_2$ does not increase, while the volume fraction of amorphous phase increases. This suggests that, in this pressure range, the enthalpy of formation of the amorphous phase is less than that of the tetragonal $FeSb_2$ phase. On the other hand, as shown in Fig. 4, for pressures above 23.3 GPa, the volume fraction of amorphous phase decreases. This suggests that for pressures higher than 23.3 GPa, the enthalpy of formation of the tetragonal $FeSb_2$ phase is less than that of the amorphous phase. Unfortunately, the XRD patterns were measured up to 28.2 GPa only. However, as will be seen later, the RS spectra measured for pressures higher than 21 GPa show that a new $FeSb_2$ phase is emerging.

The XRD pattern measured for pressures equal to and higher than 14.3 GPa were simulated by the Rietveld method [21,22], considering only the orthorhombic $FeSb_2$ phase and its coexistence with a tetragonal $FeSb_2$ phase. However, for pressures higher than 21 GPa, the peaks corresponding to the tetragonal $FeSb_2$ phase are apparently less intense. A possible explanation for this is the following: with increasing pressure, the intensity of the halo of amorphous phase decreases, suggesting its decomposition or transformation into a new high pressure phase. If a transformation occurred, the diffraction peaks belonging to the new phase should appear and this is not observed. This suggests that the amorphous phase decomposes into a mixture of Fe and Sb atoms, in which the crystals of the high pressure tetragonal $FeSb_2$ phase are embedded, making its observation difficult. In order to illustrate the quality of simulations, Fig. 12 shows the simulated XRD pattern at 14.3 GPa. From this figure, one can see that the measured XRD pattern (open circles) is better reproduced by considering the coexistence of two phases, as shown in insets I1 and I2. The simulation considering only the orthorhombic $FeSb_2$ phase was not able to reproduce the shoulders at about $2\theta = 14.96^\circ$ and 18.31°. The refined structural parameters for the tetragonal $FeSb_2$ phase are summarized in Table 2. Neon gas was used as pressure-transmitting medium. According to the literature, it crystallizes in a f.c.c structure at about 10 GPa [26]. In Fig. 3, at 14.3 GPa, the two diffraction peaks at about $2\theta = 19.7^\circ$ and 22.8° were indexed to (1 1 1) and (2 0 0) planes of cubic neon (N). The latter peak is better visible for pressures higher than 15.6 GPa. The cubic neon phase was taken into account for the XRD simulations.

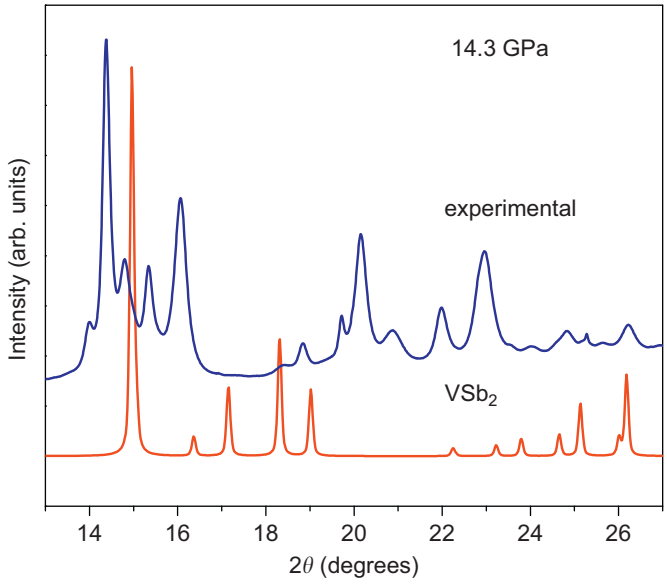

Fig. 11. XRD patterns for the nanostructured $FeSb_2$ powder measured at 14.3 GPa (top curve) and for the tetragonal VSb_2 phase using the calculated lattice parameters given in the text (bottom curve).

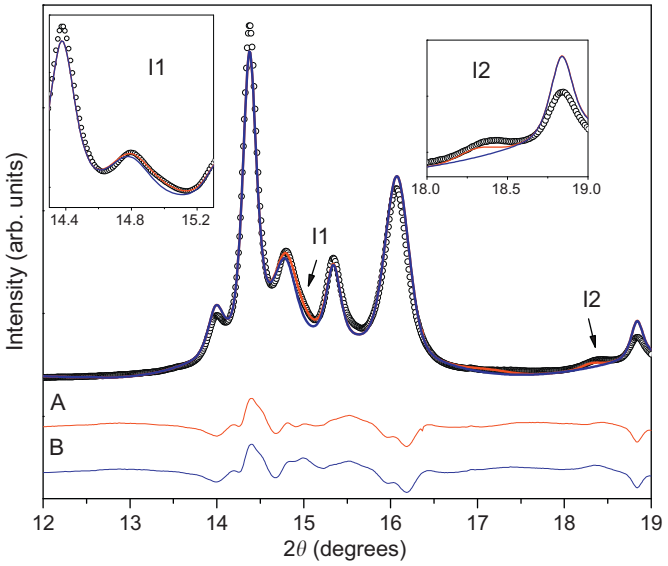

Fig. 12. XRD patterns of nanostructured $FeSb_2$ powder measured at 14.3 GPa (open circles) and simulated using the orthorhombic and tetragonal $FeSb_2$ phases (red solid line) and the orthorhombic $FeSb_2$ phase (blue solid line) only. Residual intensities (bottom line) are also shown. The refined structural parameters are listed in Table 2. (For interpretation of the references to color in this figure legend, the reader is referred to the web version of this article.)

3.3. Raman measurements under pressure

Fig. 13 shows the RS spectra with increasing pressure for nanostructured $FeSb_2$, while Fig. 14 displays the RS spectra with decreasing pressure. A comparison between these figures shows clearly the presence of new $FeSb_2$ phase. This phase is well isolated in Fig. 14 for pressures between 36.7 and 40.8 GPa. With decreasing pressure, it transforms into the orthorhombic $FeSb_2$ phase. Detailed analysis of RS spectra of the high pressure $FeSb_2$ phase will be done later.

As shown in Sections 3.1 and 3.2, the microstructure of the as-milled powder is formed by elemental rhombohedral Sb, orthorhombic $FeSb_2$ and an amorphous phase. At ambient conditions, the elemental rhombohedral Sb has the Raman active modes $E_g \approx 110\ cm^{-1}$ and $A_{1g} \approx 150\ cm^{-1}$. The effect of high pressure on these Raman active modes has been widely studied [34,35]. It was reported that, with increasing pressure up to the first phase transition (≈ 6 GPa), the Raman modes shift to smaller wave numbers. In Fig. 13, the Raman active modes of Sb are identified with an asterisk (*). With increasing pressure, the same

Table 2
Tetragonal $FeSb_2$ high pressure refinements: lattice parameters, volume, Fe atom at 4a site at (0,0,1/4), coordinates x and y of the Sb atom at 8h site at (x,y,0).

P (GPa)	14.3	15.6	17.6	19.1	21	23.3	28.2
a (Å)	6.8441	6.8315	6.8227	6.8032	6.7985	6.7761	6.7210
c (Å)	5.2563	5.2328	5.1902	5.1569	5.1310	5.1120	5.0723
V (Å^3)	246.21(4)	244.21(1)	241.59(9)	238.67(9)	237.15(2)	234.72(0)	229.13(0)
Sb (x)	0.1233(1)	0.1350(2)	0.1350(1)	0.1349(1)	0.1558(8)	0.1677(2)	0.1739(0)
Sb (y)	0.6233(1)	0.6350(2)	0.6350(1)	0.6349(1)	0.6558(8)	0.6677(2)	0.6739(0)

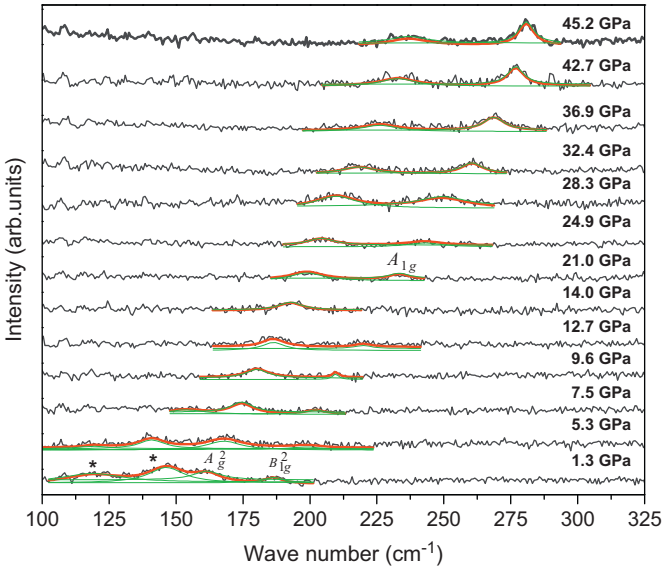

Fig. 13. Raman spectra measured with increasing pressure up to 45.2 GPa for the nanostructured orthorhombic $FeSb_2$ powder. The excitation wavelength was λ=514.5 nm. Raman active modes from unreacted antimony are marked with the asterisk (*) symbol. The red and green full lines represent the deconvolution process (see text). (For interpretation of the references to color in this figure legend, the reader is referred to the web version of this article.)

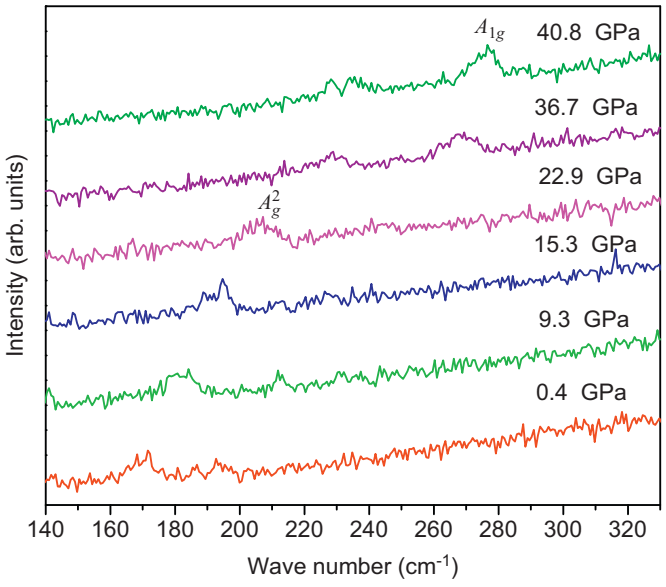

Fig. 14. Raman spectra measured with decreasing pressure for the nanostructured orthorhombic $FeSb_2$ powder. The excitation wavelength was λ=514.5 nm.

behavior mentioned in the literature is observed, and for pressures higher than 5.3 GPa they are no longer observed, suggesting that the elemental Sb was incorporated to $FeSb_2$ and/or the amorphous phase. With decreasing pressure, the Raman active modes of Sb are not recovered.

The normal modes of orthorhombic $FeSb_2$ at the Γ point of the Brillouin zone are classified according to the irreducible representations of this point group [36]:

$$\Gamma = 2A_g + 2B_{1g} + B_{2g} + B_{3g} + B_{1u} + 3B_{2u} + 3B_{3u} \quad (2)$$

where g and u denote Raman active and infrared modes, respectively.

Lazarevic et al. [36] reported the Raman spectrum of the orthorhombic $FeSb_2$ phase at room temperature, and the wave numbers are A_g^1=146.8 cm^{-1}, A_g^2=161.2 cm^{-1}, B_{1g}^1=173.3 cm^{-1}, B_{1g}^2=184.3 cm^{-1}, B_{2g}=89.4 cm^{-1} and B_{3g}=95.6 cm^{-1}. The wave number values for the IR modes are also given in Ref. [36]. The peaks centered at about 163 and 187 cm^{-1} on the Raman spectrum measured at 1.3 GPa seen in Fig. 13 were attributed to the A_g^2 and B_{1g}^2 modes, respectively. With increasing pressure, the B_{1g}^2 mode shifts to higher wave numbers, and for pressures higher than 14.0 GPa, it is no longer observed. With increasing pressure, the A_g^2 mode shifts to higher wave numbers, becomes enlarged and less intense. On the other hand, at about 21 GPa, a new Raman active mode at about 233.4 cm^{-1} emerges, becoming sharper and intense for higher pressures. This indicates the growth of a new $FeSb_2$ phase. With decreasing pressure up to 36.7 GPa, only the Raman active modes belonging to the new high pressure $FeSb_2$ phase are observed. For smaller pressures, it transforms into the orthorhombic $FeSb_2$ structure.

At ambient conditions, the angle [Sb(10)–Fe(7)–Sb(12)] is smaller than the [Sb(10)–Fe(7)–Sb(11)] angle (see Fig. 1). Therefore, the interatomic distance Sb(10)–Sb(12) is smaller than the Sb(10)–Sb(11) distance. The interatomic distance Fe(7)–Sb(10) is smaller than the Fe(7)–Sb(12) distance. Fig. 9 shows that, with increasing pressure, the angle [Sb(10)–Fe(7)–Sb(12)] shows a minimum and a maximum at 12.6 and 21 GPa, respectively. The opposite is observed for the angle [Sb(10)–Fe(7)–Sb(11)]. Fig. 10 shows that, at 12.6 GPa, the interatomic distance Fe(7)–Sb(10) displays a minimum and the Fe(7)–Sb(12) distance displays a maximum. Physically, the bond Fe(7)–Sb(10) becomes stronger and Fe(7)–Sb(12) becomes weaker. Topologically, a significant deformation of the already deformed octahedral is promoted. In addition, the interatomic distance Sb(10)–Sb(12) shows a minimum at 12.6 GPa, indicating that the balance of the attractive and repulsive terms of the bond favors the cohesion energy. A combination of all these facts seems to be responsible for the increase in the structural stability of $FeSb_2$ observed at about 14.3 GPa as shown in Fig. 5. The presence of defective chemical bonds as well as the breaking of some of these bonds seem to be responsible for the enlargement and the loss of intensity observed in the Raman active modes displayed in Fig. 13; decomposition of the $FeSb_2$ phase seen in Fig. 5, the increase of the volume fraction of the amorphous phase; and the nucleation of the tetragonal $FeSb_2$ phase, which did not grow due to the presence of amorphous phase, as suggested by the Rietveld analysis of the XRD patterns measured for pressures higher than 14.3 GPa.

The XRD patterns for pressures between 14.3 and 28.2 GPa show the presence of the tetragonal and orthorhombic $FeSb_2$ phases. Fig. 13 shows that for pressures higher than 21.0 GPa a new phase starts to form and, as shown in Fig. 14, the volume fraction of this phase is larger for pressures above 22.9 GPa. At ambient conditions, the compounds $TiSb_2$, VSb_2, $MnSn_2$, $CoSn_2$, $FeSn_2$ crystallize in a $CuAl_2$ structure-type (symmetry D_{4h}^{18}) [3]. For these compounds, the Raman active modes at the Γ point of the Brillouin zone are classified according to the irreducible representations of this point group [37]:

$$\Gamma = A_{1g} + B_{1g} + B_{2g} + 2E_g \quad (3)$$

Armbruster et al. [37,38] reported the Raman spectra at room conditions for the $TiSb_2$ and VSb_2 compounds, in form of powders and single crystals. For $TiSb_2$ powders, the wave numbers of Raman active modes are $A_{1g}=172\ cm^{-1}$, $B_{1g}=129\ cm^{-1}$, $B_{2g}=180\ cm^{-1}$, $E_{1g}=83\ cm^{-1}$ and $E_{2g}=254\ cm^{-1}$, while for VSb_2 powders they are $A_{1g}=166\ cm^{-1}$, $B_{1g}=116\ cm^{-1}$, $B_{2g}=176\ cm^{-1}$, $E_{1g}=103\ cm^{-1}$ and $E_{2g}=229\ cm^{-1}$. The A_{1g} mode is the most intense, while the B_{1g} and E_g modes form a broad band. Assuming that the new $FeSb_2$ phase observed in Figs. 13 and 14 crystallizes in a $CuAl_2$ structure-type, it is possible to estimate the wave number at ambient conditions for its most intense Raman active A_{1g} mode by fitting this Raman peak between 21 and 45.2 GPa to a standard second order polynomial. The calculated value was $169\ cm^{-1}$, which is in reasonable agreement with the results reported in Refs. [37,38] for the tetragonal phase at ambient conditions.

The pressure dependence of the wave number of the A_{2g} mode of the orthorhombic and of the A_{1g} mode of the tetragonal $FeSb_2$ phase was approximated by a standard second order polynomial as shown in Fig. 15. The maxima of the modes were obtained by deconvolution using the Lorentzian functions. Based on the XRD patterns and the RS spectra recorded with increasing pressure, the wave numbers for the orthorhombic phase up to 28.3 GPa and for the tetragonal phase from 21.0 to 45.2 GPa are given by

$$\varpi(P)A_g^2 = 157.439 + 2.507P - 0.024P^2 \quad \text{(orthorhombic phase)}$$

$$\varpi(P)A_{1g} = 169.062 + 3.441P - 0.021P^2 \quad \text{(tetragonal phase)} \quad (4)$$

The Grüneisen parameter γ_0 describes the effect of pressure on the volume of the lattice, and consequently, on the phonons frequencies. The zero-pressure mode Grüneisen parameters γ_0 were determined using the equation [39,40]

$$\gamma_0 = \frac{B_0}{\omega_0}\left(\frac{\partial\omega}{\partial P}\right)_{P=0} \quad (5)$$

where B_0 and ϖ_0 are the bulk modulus in GPa and the wave number in cm^{-1} at zero pressure. From the XRD measurements, a value of $B_0=75.5\pm3.2$ GPa for the orthorhombic $FeSb_2$ phase was obtained, while Wu et al. [5] reported $B_0=68$ GPa for the tetragonal $FeSb_2$ phase. Using B_0 and ϖ_0 values in Eq. (5), the γ_0 values for the A_g^2 and A_{1g} modes are 1.17 and 1.38, respectively.

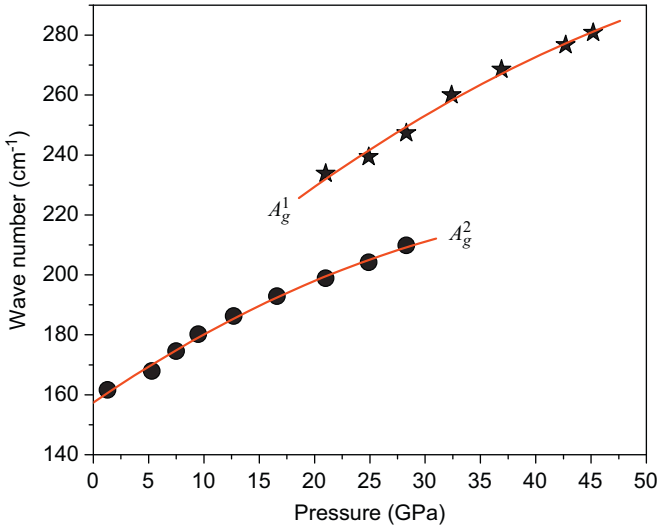

Fig. 15. Experimental pressure dependence of the Raman mode frequencies for the orthorhombic (full circles) and tetragonal (full stars) $FeSb_2$ phases.

4. Conclusions

The structural and optical properties of nanostructured orthorhombic $FeSb_2$ formed by the MA technique were studied for several applied pressures, and the main conclusions are (1) the XRD results show the presence of an orthorhombic $FeSb_2$ phase up to 28.2 GPa, (2) with increasing pressure, the orthorhombic $FeSb_2$ phase decomposes, promoting an increase in the volume fraction of an amorphous phase up to 23.3 GPa. The latter also decomposes at higher pressures, (3) for pressures higher than 14.3 GPa, the XRD patterns show a mixture of orthorhombic and tetragonal $FeSb_2$ phases, (4) for pressures above 21 GPa, the RS spectra show the presence of a tetragonal $FeSb_2$ phase. With decreasing pressure down to 36.7 GPa, the Raman peaks seen on the RS spectra are attributed to this high pressure phase. For smaller pressures, it transforms into an orthorhombic $FeSb_2$ phase, and (5) considering the RS spectra for the tetragonal $TiSb_2$ and VSb_2 powders, the most prominent Raman peak seen between 21.0 and 45.2 GPa in Figs. 13 and 14 is attributed to the Raman active A_{1g} mode of a tetragonal phase.

Acknowledgments

This research was financially supported by the Brazilian–French CAPES/COFECUB Program (Project no. 559/7). We thank ELETTRA synchrotron (Italy) for the XRD measurements as a function of pressure. We are indebted to Jean-Claude Chervin, Pascal Munch and Gilles Le Marchand for technical support. We are also indebted to Dr. Altair Sória Pereira and Dr. Ronaldo Sergio de Biasi for suggestions and careful reading of the manuscript.

References

[1] A. Bentien, S. Johnsen, G.K.H. Madsen, B.B. Iversen, F. Steglich, Europhys. Lett. 80 (2007) 17008.
[2] R. Hu, V.F. Mitrović, C. Petrovic, Appl. Phys. Lett. 92 (2008) 182108.
[3] ICSD—Inorganic Crystal Structure Database, Gmelin-Institut fur Anorganische Chemie and Fachinformationszentrum FIZ Karlsruhe, 1995 Joint Committee on Powder Diffraction Standards (JCPDS), Philadelphia, 2000.
[4] C. Petrovic, Y. Lee, T. Vogt, N.Dj. Lazarov, S.L. Bud'ko, P.C. Canfield, Phys. Rev. B 72 (2005) 045103.
[5] X. Wu, G. Steinle-Neumann, S. Qin, M. Kanzaki, L. Dubrovinsky, J. Phys.: Condens. Matter 21 (2009) 185403.
[6] C.E.M. Campos, J.C. de Lima, T.A. Grandi, K.D. Machado, J.P. Itié, A. Polian, J. Phys.: Condens. Matter 16 (2004) 8485.
[7] C.E.M. Campos, J.C. de Lima, T.A. Grandi, J.P. Itié, A. Polian, Solid State Ionics 176 (2005) 2639.
[8] C.E.M. Campos, J.C. de Lima, T.A. Grandi, K.D. Machado, J.P. Itié, A. Polian, J. Solid State Chem. 178 (2005) 93.
[9] A. Polian, M. Gauthier, S.M. Souza, D.M. Trichês, J.C. de Lima, T.A. Grandi, Phys. Rev. B 83 (2011) 113106.
[10] D.M. Trichês, S.M. Souza, J.C. de Lima, T.A. Grandi, C.E.M. Campos, A. Polian, J.P. Itié, F. Baudelet, J.C. Chervin, J. Appl. Phys. 106 (2009) 013509.
[11] H. Gleiter, Nanostruct. Mater. 1 (1992) 1.
[12] C. Suryanarayana, Prog. Mater. Sci. 46 (2001) 1.
[13] J.C. de Lima, D.M. Trichês, V.H.F. dos Santos, T.A. Grandi, J. Alloys Compd. 282 (1999) 258.
[14] R.B. Schwarz, R.R. Petrich, C.K. Saw, J. Non-Cryst. Solids 76 (1985) 281.
[15] H.J. Fecht, Acta Metall. Mater. 38 (1990) 1927.

[16] J.C. de Lima, V.H.F. dos Santos, T.A. Grandi, P.C.T. D'Ajello, A. Dmitriev, Phys. Rev. B 62 (2000) 8871.
[17] J.C. Chervin, B. Canny, J.M. Besson, Ph. Pruzan, Rev. Sci. Instrum. 66 (1995) 2596.
[18] J.C. Chervin, B. Canny, M. Mancinelli, High Pressure Res. 21 (2001) 305.
[19] E. Bussetto, A. Lausi, A. Paverse, Sincrotrone Trieste, Seventh Users Meeting, ICTP, Trieste, Italy, 1999, p. 29.
[20] A.P. Hammersley, S.O. Svensson, M. Hanfland, A.N. Fitch, D. Hausermann, High Pressure Res. 14 (1996) 235.
[21] H.M. Rietveld, J. Appl. Crystallogr. 2 (1969) 65.
[22] A.C. Larson, R.B. Von Dreele, Los Alamos National Laboratory Report LAUR 86-748, 2004.
[23] B.D. Cullity, Elements of X-Ray Diffraction, Second Edition, Addison-Wesley Publishing Company, Inc., Philippines, 1978.
[24] C.M. Poffo, J.C. de Lima, S.M. Souza, D.M. Trichês, T.A. Grandi, R.S. de Biasi, J. Raman Spectrosc. 41 (2010) 1316.
[25] S.M. Souza, D.M. Trichês, J.C. de Lima, T.A. Grandi, R.S. de Biasi, Physica B 405 (2010) 2807.
[26] R.J. Hemley, C.S. Zha, A.P. Jephcoat, H.K. Mao, L.W. Finger, D.E. Cox, Phys. Rev. B 39 (1989) 11820.
[27] K. Syassen, Computer code DATLAB Max Planck Institute, Stuttgart, Germany, 2003.
[28] C.C. Koch, O.B. Cavin, C.G. McKamey, J.O. Scarbrough, Appl. Phys. Lett. 43 (1983) 1017.
[29] TAPP Software, Version 2.2, E.S. Microwave Inc., Wade Court, Hamilton, OH.
[30] F. Birch, Phys. Rev. 71 (1947) 809.
[31] H.J. Fecht, Acta Metall. Mater. 38 (1990) 1927.
[32] Atomic Softek, Crystal Office 98 Sotfware Hamilton, Ontario, Canada.
[33] H. Takizawa, K. Uheda, T. Endo, J. Alloys Compd. 287 (1999) 145.
[34] X. Wang, K. Kunc, I. Loa, U. Schwarz, K. Syassen, Phys. Rev. B 74 (2006) 134305.
[35] O. Degtyareva, V.V. Struzhkin, R.J. Hemley, Solid State Commun. 141 (2007) 164.
[36] N. Lazarevic, M.M. Radonjic, D. Tanaskovic, R. Hu, C. Petrovic, Z.V. Popovic, J. Phys.: Condens. Matter 24 (2012) 255402.
[37] M. Armbruster, W. Schnelle, U. Schwarz, Y. Grin, Inorg. Chem. 46 (2007) 6319.
[38] Y. Grin, F.R. Wagner, M. Armbruster, M. Kohout, A. Leithe-Jasper, U. Schwarz, U. Wedig, H.G. Schnering, J. Solid State Chem. 179 (2006) 1707.
[39] M. Blackman, Proc. Phys. Soc. B 70 (1957) 827.
[40] W.B. Daniels, Lattice Dynamics, in: R.F. Wallis (Ed.), Pergamon, Oxford, 1965, p. 273.